Adaptive resolution simulations coupling atomistic water to dissipative particle dynamics

Julija Zavadlav, and Matej Praprotnik

Adaptive resolution simulations coupling atomistic water to dissipative particle dynamics

Julija Zavadlav[1,2] and Matej Praprotnik[2,3,a)]

[1]*Chair of Computational Science, ETH Zürich, Clausiusstrasse 33, CH-8092 Zurich, Switzerland*
[2]*Department of Molecular Modeling, National Institute of Chemistry, Hajdrihova 19,
SI-1001 Ljubljana, Slovenia*
[3]*Department of Physics, Faculty of Mathematics and Physics, University of Ljubljana, Jadranska 19,
SI-1000 Ljubljana, Slovenia*

Multiscale methods are the most efficient way to address the interlinked spatiotemporal scales encountered in soft matter and molecular liquids. In the literature reported hybrid approaches span from quantum to atomistic, coarse-grained, and continuum length scales. In this article, we present the hybrid coupling of the molecular dynamics (MD) and dissipative particle dynamics (DPD) methods, bridging the micro- and mesoscopic descriptions. The interfacing is performed within the adaptive resolution scheme (AdResS), which is a linear momentum conserving coupling technique. Our methodology is hence suitable to simulate fluids on the micro/mesoscopic scale, where hydrodynamics plays an important role. The presented approach is showcased for water at ambient conditions. The supramolecular coupling is enabled by a recently developed clustering algorithm SWINGER that assembles, disassembles, and reassembles clusters as needed during the course of the simulation. This allows for a seamless coupling between standard atomistic MD and DPD models. The developed framework can be readily applied to various applications in the fields of materials and life sciences, e.g., simulations of phospholipids and polymer melts, or to study the red blood cells behavior in normal and disease states. *Published by AIP Publishing.* https://doi.org/10.1063/1.4986916

I. INTRODUCTION

Proper treatment of hydrodynamics is a highly desirable if not imperative feature in simulations of many physical processes of interest, especially those pertaining to systems under flow and/or non-equilibrium conditions. Consequently, various simulation techniques have been proposed that uphold the hydrodynamic conservation laws. On the mesoscopic (e.g., coarse-grained) level, the particle-based methods are, for example, the dissipative particle dynamics (DPD) method,[1–8] the multiparticle collision dynamics (MPC),[9] and smoothed dissipative particle dynamics (SDPD).[10,11] In the DPD, lumps of atoms/molecules are grouped to form soft beads that interact via explicit soft conservative, random, and dissipative forces to simulate fluids on a mesoscopic scale with correct hydrodynamics interactions. In the SDPD, the Navier-Stokes equations are numerically solved with a formalism that is reminiscent of molecular dynamics (MD), whereas in the MPC, the system is modeled by particles with continuous positions and velocities and stochastic interparticle interactions.

One can also view the DPD as a local linear momentum-preserving thermostat to MD[12,13] for application to "hard" atomistic systems, where the forces from a corresponding MD force field are used as conservative forces in the DPD instead of soft linear repulsive forces between soft particles in its original formulation. In general, the dynamics observed

with mesoscopic models is faster compared with atomistic MD due to much smoother energy landscapes. In the formal derivation of equations of motion for the coarse-grained degrees of freedom guaranteeing the proper dynamics, one resorts to Mori-Zwanzig formalism[14–19] resulting in the generalized Langevin equation. Unfortunately, the latter is usually numerically unsolvable and one has to make several approximations, e.g., memory effects are usually neglected. Transport properties can then be tuned by changing the friction coefficients of the thermostat.[13,20]

The micro- and mesoscopic approaches often lead to trade-offs, i.e., the reduced computational load gained in mesoscopic methods, which facilitates accessibility to larger spatiotemporal scales, comes at the expense of the elimination of some degrees of freedom present in the microscopic approaches.[21,22] Contrarily, the combined micro-meso simulation framework can leverage the advantages from both. This reasoning led to the development of recent hybrid approaches, where the system is spatially decomposed into a region of interest, modeled with MD and the rest of the system modeled with a mesoscopic approach.[23–29] The interfacing of simulation techniques has to be constructed in such a way that the linear momentum is preserved across all domains. Hence, the approaches so far are either based on or adopt a similar coupling strategy as the adaptive resolution scheme (AdResS).[23,24,30] For example, using AdResS Petsev *et al.*[31] coupled the MD to SDPD, whereas Alekseeva *et al.*[32] linked the MD with MPC. The robustness of both hybrid approaches was demonstrated on a Lennard-Jones fluid.

a)praprot@cmm.ki.si

The on-the-fly coupling of the MD and DPD methods has not been demonstrated yet and is the purpose of this work. In particular, we consider bulk water at ambient conditions employing the multimolecular mapping, i.e., multiple water molecules are modeled as soft beads in the DPD domain. Such coupling requires two considerations. First, there is an upper limit (maximum number of molecules N_m^{max} representing one DPD particle) on the level of coarse-graining at which the physical properties can still be modeled in an efficient manner. This issue was examined in significant detail by Pivkin and Karniadakis[33] where N_m^{max} was found to be below 20. Second, special consideration has to be put forth regarding the coupling of free-particle groups (multimolecular mapping) as opposed to bound particles of multi-site molecules (monomolecular mapping). Namely, molecules in the MD domain naturally diffuse in time (in the case of water the clusters are reformed on a picosecond timescale). Thus, if one wishes to map more than one molecule always to the same DPD bead, the motion of those molecules with respect to the DPD site must be restricted.[34,35] While these shortcuts simplify the supramolecular coupling, they also cause in certain situations spurious artifacts, such as partial unfolding of biomolecules.[36] To overcome this limitation, we have developed a clustering algorithm SWINGER[37] that redistributes molecules into clusters on-the-fly thus allowing a seamless coupling between standard atomistic and supramolecular water models. The algorithm was first applied to connect the atomistic and the well-established MARTINI coarse-grained force field[38–40] and paved the way for efficient MD simulations of biomolecular systems.

In this work, we employ SWINGER in conjunction with AdResS to couple MD and DPD regimes thus breaking ground for future hydrodynamics studies. We test two supramolecular couplings, i.e., the 4-to-1 mapping aimed at future applications to phospholipids[41] and 8-to-1 mapping aimed at future applications to polymer melts.[42] The adequateness of the MD/DPD coupling is demonstrated on the reproducibility of several equilibrium structural and dynamical properties of the monoscale simulations.

II. MODELS AND METHODS

In this section, we introduce the on-the-fly coupling of atomistic MD and DPD water models via the multiscale scheme AdResS and clustering algorithm SWINGER (Fig. 1). We perform all our simulations in thermodynamical equilibrium, i.e., no fluid flows are present.

A. Molecular dynamics (MD) domain

In the MD region, we employ the three-site SPC water model,[43] with the Lennard-Jones (LJ) interaction between oxygen atoms and intermolecular electrostatic interactions. The force between atoms i and j at positions $\mathbf{r}_i$ and $\mathbf{r}_j$ is given by

$$\mathbf{F}_{ij}^{MD,C}(\mathbf{r}_{ij}) = -\frac{\partial U^{MD}}{\partial \mathbf{r}_{ij}}, \tag{1}$$

where $\mathbf{r}_{ij} = \mathbf{r}_i - \mathbf{r}_j$. The geometry of the water molecules is constrained with SETTLE.[44] The cutoff distance for the nonbonded interactions is $r_c = 0.9$ nm. They are capped for
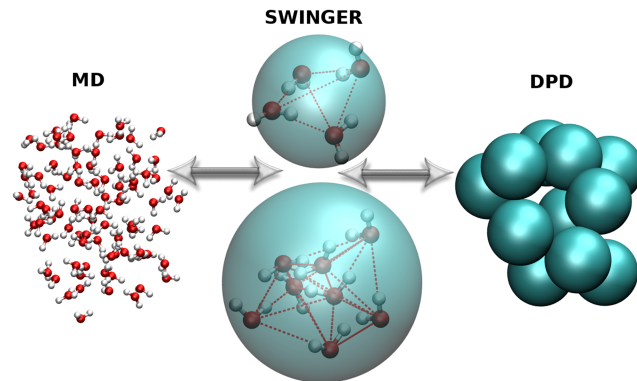

FIG. 1. Coupling of MD and DPD methods via AdResS interfacing and dynamic clustering algorithm SWINGER. The coupling is concurrent, i.e., the molecules change their representation on-the-fly as they diffuse through different domains in the system.

very short distances (at 0.17, 0.08, and 0.14 nm, for the oxygen-oxygen, oxygen-hydrogen, and hydrogen-hydrogen interactions, respectively), i.e., at distances where the corresponding radial distribution function is still zero. The reaction field method[45] is used for the electrostatic interaction beyond the cutoff, with the dielectric permittivity of the inner and outer region equal to 1 and 80, respectively. The temperature is maintained at 300 K with a local linear momentum preserving DPD thermostat[12] with a coupling constant of 0.125 a.u./ps and a cutoff radius equal to the cutoff radius of non-bonded interactions.

B. Dissipative particle dynamics (DPD) domain

In the particle-based mesoscopic DPD method,[1] the particles α and β interact via short-ranged repulsive forces ($\mathbf{F}_{\alpha\beta}^{DPD,C}$), random forces ($\mathbf{F}_{\alpha\beta}^{DPD,R}$), and dissipative forces ($\mathbf{F}_{\alpha\beta}^{DPD,D}$) defined as follows:

$$\mathbf{F}_{\alpha\beta}^{DPD,C}(\mathbf{R}_{\alpha\beta}) = a_{\alpha\beta}(1 - R_{\alpha\beta}/R_c)\hat{\mathbf{R}}_{\alpha\beta},$$

$$\mathbf{F}_{\alpha\beta}^{DPD,R}(\mathbf{R}_{\alpha\beta}) = \sqrt{2\gamma_{\alpha\beta}k_BT}(1 - R_{\alpha\beta}/R_c)\zeta_{ij}\hat{\mathbf{R}}_{\alpha\beta}, \tag{2}$$

$$\mathbf{F}_{\alpha\beta}^{DPD,D}(\mathbf{R}_{\alpha\beta}) = -\gamma_{\alpha\beta}(1 - R_{ij}/R_c)^2(\hat{\mathbf{R}}_{\alpha\beta} \cdot \mathbf{V}_{\alpha\beta})\hat{\mathbf{R}}_{\alpha\beta}.$$

Here, the vectors $\mathbf{R}_{\alpha\beta} = \mathbf{R}_\alpha - \mathbf{R}_\beta$ and $\mathbf{V}_{\alpha\beta} = \mathbf{V}_\alpha - \mathbf{V}_\beta$ are, respectively, the position and velocity differences between particles α and β. The parameters $\gamma_{\alpha\beta}$ are the friction coefficients and $\zeta_{\alpha\beta}$ are symmetric Gaussian random variables with zero mean and unit variance. The particles interact only for separation distances $R_{\alpha\beta} < R_c$, where the R_c is the diameter of the particles. The DPD force, as defined by Eq. (2), satisfies Newton's third law and hence conserves the local linear momentum.

In this work, we use 4-to-1 and 8-to-1 mapping schemes. Therefore, each DPD particle has a mass M and effective volume comparable to N_m water molecules, where N_m is either 4 or 8. The effective diameter R_c (in nm) of DPD particles is set by $R_c = 0.3107\sqrt[3]{\bar{\rho}N_m/\rho_w(T)}$, where $\bar{\rho}$ is the DPD number density defined as the number of beads contained in a cube of volume R_c^3 and $\rho_w(T)$ is the mass density of liquid water (in g cm^{-3}) at the temperature T. For $\bar{\rho} = 3$ and $N_m = 4$ and 8 this gives $R_c = 0.71$ and 0.896 nm, respectively. The repulsion strengths a_{ij} are usually defined by $a = (N_m\kappa^{-1} - 1)/2\alpha\bar{\rho}$

(in units of $k_b T/R_c$) to reproduce the compressibility κ of the system.[1] Liquid water at room temperature has a compressibility of $\kappa_{\exp}^{-1} \approx 16$. By substituting the values $N_m = 4$, 8 and $\alpha = 0.101$, one finds $a \approx 100$[41] and 200,[42] respectively. The friction coefficient is set with $\gamma = 4.5\sqrt{Mk_bT}/R_c$.[42]

As already mentioned in the Introduction, we could use another conservative force instead of a linear function for $\boldsymbol{F}_{\alpha\beta}^{DPD,C}$. For example, soft effective coarse-grained pairwise interactions between soft blobs can be obtained by the Boltzmann iteration procedure[46,47] to reproduce the radial distribution functions from reference all-atom MD simulations as has been done in Refs. 48–50 for a star-polymer melt. This would correspond to a situation where DPD is used as a thermostat to MD.[12,13] However, our very aim in this work is to couple atomistic water with the original DPD water model using the linear conservative force as described above.

C. Adaptive resolution scheme (AdResS)

The MD and DPD domains are coupled via a force interpolation scheme, which is linear momentum conservative as it upholds Newton's third law.[23,24] The force acting between DPD particles, which are a coarser representation of N_m water molecules clusters, α and β is

$$\boldsymbol{F}_{\alpha\beta} = \left[1 - w(X_\alpha)w(X_\beta)\right]\boldsymbol{F}_{\alpha\beta}^{MD,C} + w(X_\alpha)w(X_\beta)\boldsymbol{F}_{\alpha\beta}^{DPD,C}. \quad (3)$$

The $\boldsymbol{F}_{\alpha\beta}^{MD,C}$ and $\boldsymbol{F}_{\alpha\beta}^{DPD,C}$ are the conservative forces between particles α and β defined by Eqs. (1) and (2) and $\boldsymbol{F}_{\alpha\beta}^{MD,C}$ = $\sum_{i\alpha,j\beta} \boldsymbol{F}_{i\alpha j\beta}^{MD,C}$, where the sum runs over all pair interactions between explicit atoms (denoted by the running index $i\alpha$) of the DPD particle α and explicit atoms (denoted by the running index $j\beta$) of the DPD particle β. The $X_{\alpha,\beta}$ is the distance of DPD particle α, β to the center of the MD region. In the MD domain, where the DPD particles do not exist, the forces are purely atomistic as in the standard all-atom MD simulation.

To achieve a smooth coupling between resolution domains, we introduce a weighting function $w \in [0, 1]$, which depends on the position of the DPD particle. In the MD and DPD domains, w takes the extreme values of 0 and 1, respectively. The intermediate values correspond to the HY region ($X_{MD} < X < X_{DPD}$) where w has the following form:

$$w(X) = \cos^2\left[\frac{\pi(X_{DPD} - X)}{2(X_{DPD} - X_{MD})}\right]. \quad (4)$$

Note, that in the standard AdResS scheme, a reversed definition of w function is used, i.e., it is equal to 1 in the high resolution domain and 0 in the low resolution domain. Our methodology can, therefore, be coined a "reverse" AdResS scheme. In the standard scheme, a direct interaction among all-atom and hybrid molecules is present up to one potential cutoff deep into the MD domain. Therefore, it requires a definition of the DPD interaction sites in this part of the MD domain. In other words, the original implementation of AdResS requires an enlarged MD region where the water molecules in the clusters are constrained to remain first neighbors as in, for example, bundled-SPC water model. From a computational point of view, such implementation is not optimal as one would like
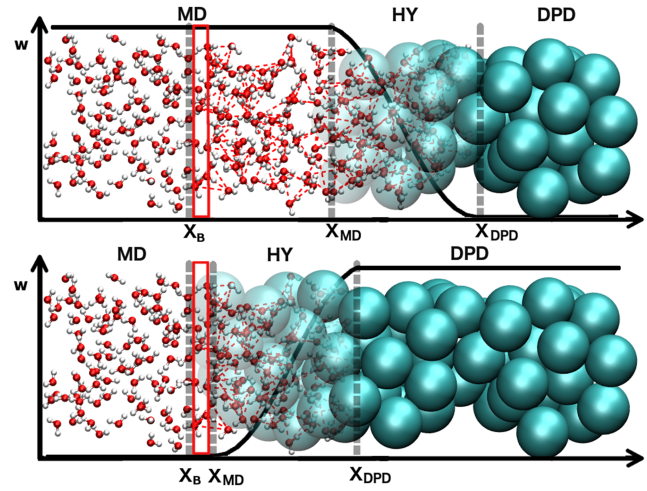

FIG. 2. Original (top) and "reverse" (bottom) weighting functions used to smoothly couple the MD and DPD methods. In this work, we use the "reverse" version, where $w = 0$ and 1 in the MD and DPD domains, respectively. Boundaries between the regions are marked with dotted gray lines, whereas the region C, where the clusters are formed, is framed with red lines.

to minimize the computationally heavy MD region. Hence, in this work, we resort to the reverse AdResS. The comparison of both schemes is shown in Fig. 2 where we schematically depict half of the simulation box with the MD region located at the center of the simulation box. At equal size of the MD region with unconstrained water molecules, the reverse implementation allows one to shift the HY region closer to the MD domain. Consequently, the ratio between the sizes of DPD and MD region is enlarged, which results in higher computational speed-up.

To compensate the difference in the chemical potentials of the MD and DPD resolutions, we employ a thermodynamic (TD) force F^{TD},[51,52] so that the total force acting on a given DPD particle α reads as

$$\boldsymbol{F}_\alpha = \sum_{\beta \neq \alpha} \left\{ \left[1 - w(X_\alpha)w(X_\beta)\right] \boldsymbol{F}_{\alpha\beta}^{MD,C} \right.$$
$$\left. + w(X_\alpha)w(X_\beta)\boldsymbol{F}_{\alpha\beta}^{DPD,C} \right\} - \boldsymbol{F}_\alpha^{TD}(X_\alpha). \quad (5)$$

F^{TD} is applied on DPD particles with mass M in the HY region and it is calculated in an iterative manner as

$$F_{i+1}^{TD} = F_i^{TD} - \frac{M}{\rho_0^2 \kappa_T} \nabla \rho_i(\boldsymbol{r}), \quad (6)$$

where κ_T is the isothermal compressibility, ρ_0, the system density, and $\rho(\boldsymbol{r})$ is the nonuniform density to which the system would adjust itself to without applying an external force. From relation $(\partial\mu/\partial\rho)_{V,T} = 1/\rho_0^2\kappa_T$, we see that the TD force is compensating for the differences in the chemical potential at different levels of resolution. For further details, we refer the reader to Refs. 25 and 51–55.

Applying an external force to the system changes the linear momentum. Due to the TD force, the linear momentum is not conserved on the local atomistic level. However, in the derivation of the TD force (which acts on the centers of mass of DPD particles), there is a switch from a molecular (particle-based) to a field description. For example, center-of-mass density field is defined as $\rho(X) = M_\alpha \sum_\alpha \delta(X - X_\alpha)$ and

similarly, one defines also the pressure and chemical potential density fields, see, e.g., Refs. 54–56. Although the TD is not pairwise, it conserves local linear momentum on this (fluctuating hydrodynamics) level of description; see also Sec. III. Besides, $F^{TD} = 0$ in the region of interest, i.e., in the MD region. The local linear momentum conservation guarantees that we correctly reproduce momentum propagation, which is essential for the correct reproduction of hydrodynamic behavior.[12]

D. SWINGER

The coupling is supramolecular, i.e., 4-to-1 and 8-to-1. To facilitate such coupling, we employ the SWINGER algorithm that dynamically makes, breaks, and remakes clusters of water molecules that form DPD particles. The detailed

description of the algorithm is reported in Ref. 37. Here, we briefly summarize it for completeness. The algorithm breaks the clusters that have moved to the MD region and makes or remakes clusters in a predefined "cluster formation" region C (see Fig. 2). In this work, the region C is $X_{skin} = 0.2, 0.4$ nm (for $N_m = 4$ and 8, respectively) thick layer bordering the edge of the MD domain ($X_B = X_{MD} - X_{skin}$). The algorithm's output is an optimal grouping of water molecules into clusters, where each cluster contains exactly 4 or 8 water molecules. The optimal grouping is achieved with the initial grouping in an orderly fashion and the simulated annealing Monte Carlo (MC) based refinement. Since the typical timescale of waters' tetrahedral clusters is on the order of a ps, the SWINGER scheme is not initiated at every MD step but only at every Verlet list update. When the clusters are formed a half-harmonic spring interaction, given by

$$U_B(r_{ij}, X) = \begin{cases} \frac{1}{2}k(r_{ij} - r_0)^2, & r_{ij} > r_0; X > X_{DPD} \\ \frac{1}{2}k(r_{ij} - r_0)^2 \cos\left(\frac{\pi(X_{DPD} - X)}{2(X_{DPD} - X_B)}\right), & r_{ij} > r_0; X_B < X < X_{DPD} \\ 0, & \text{otherwise} \end{cases} \tag{7}$$

is added between the oxygen atoms within a cluster. The force-constant k is 1000 kJ mol^{-1} nm^{-2} and r_{ij} and $r_0 = 0.3$ nm are the current and equilibrium distance between oxygen atoms, respectively. For 4-to-1 mapping, all water molecules in the cluster are nearest neighbors and the half-harmonic spring interaction acts between all oxygen pairs. However, for the 8-to-1 mapping clusters contain also the second neighbors. Here, for each oxygen, the interaction is added between its 4 nearest oxygens and additionally to oxygen atoms within 0.35 nm, thus ensuring that only nearest neighbors are connected and that the cluster is well interconnected, i.e., it does not form, for example, 2 separate clusters with 4 water molecules. The bundled interaction is introduced gradually to avoid any large forces due to bundling and to accommodate an easier reclustering.

The computational cost of the SWINGER algorithm depends on the size of the clustering region. In particular, the algorithm's complexity scales linearly with M as the energy of the simulated annealing MC involves only intracluster contributions. When the algorithm is executed, the measured computational time of the MD time step is increased by approximately 5%. However, since the algorithm is, as mentioned before, not initiated at every time step, the overall increase in the computational load due to SWINGER itself is negligible.[37]

E. Simulation details

Simulations are performed with the ESPResSo++ software package.[57] For the integration, we use the standard velocity Verlet with a time step of 1 fs. We use cubic simulation box ($11.2 \times 2.8 \times 2.8$ nm^3) with periodic boundary conditions and minimum image convention. The AdResS method allows the use of different geometric boundaries between resolution regions. Here, we split the system along the x-axis so

that a $2X_{MD} = 4.8$ nm-wide MD region is at the center of the simulation box. Two HY regions, of a width of 0.9 nm each, flank the MD region. The initial system is obtained with the SWINGER algorithm, which is much more convenient than the alternative way, where the atomistic simulations are run and semi-harmonic springs are gradually added until all the clusters were formed. Production runs for all simulations are 40 ns, whereas the equilibration runs are 5 ns. As a reference, we use the conventional fully MD and DPD simulations.

III. RESULTS AND DISCUSSION

We couple the MD model of water to two DPD models with different resolutions, i.e., representing 4 and 8 water molecules. For convenience, we label these multiscale simulations AdResS 4-to-1 and AdResS 8-to-1, respectively. Additional pure atomistic MD and pure DPD simulations are labeled with MD, DPD 4, and DPD 8. The latter two correspond to the two DPD models used. In this section, we show that the structural and dynamical properties of the simulated system are well reproduced by the AdResS multiscale simulation.

First, it is known that coupling of different representations with different chemical potentials can induce density artifacts. Usually, there is a preferential tendency of molecules to migrate from high to low resolution region and change their representation in order to lower the free energy of the system. However, with the appropriate TD force, such undulations are removed. As can be observed from Fig. 3, the force profile shapes are similar for both couplings while the magnitude differs. As foreseen, larger magnitude is required for the AdResS 8-to-1 case. The TD forces have a complicated form and therefore cannot be described with simple analytical
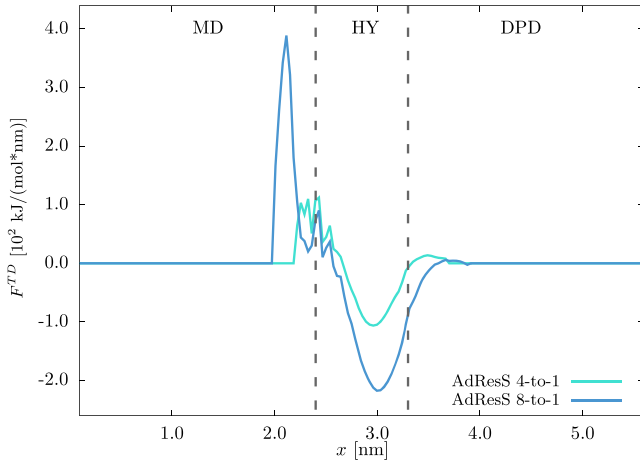
FIG. 3. Thermodynamical (TD) force applied to the DPD particles in the HY region. Vertical lines mark the domains of MD and DPD methods.

functions. Instead, we use an iterative procedure [Eq. (6)], where the correction to the force is inversely proportional to the density gradient along the direction of resolution change.[51,52] In practice, the prefactor $C = M/(\rho_0^2 \kappa_T)$ in Eq. (6) is determined empirically. To speed up the iteration procedure several simulations with different factors C are performed simultaneously at each step and the best one is used for the next iteration. Additionally, the TD force is extended into the cluster formation and DPD regions to obtain a smoother density profile. Similar extensions were used also in previous applications.[35] The convergence was obtained after 25 iterative steps. To validate the homogeneous density across different resolution regions we plot, in Fig. 4, the normalized density profile (NDP), i.e., the local density divided by the bulk density, as a function of x-position (the direction of resolution change) in the simulation box. We compute the NDPs for the water oxygen atoms and DPD particles and compare each of them with the appropriate reference MD/DPD simulation to point out that the systematic variations in the density distribution in the HY domain are well within the error bars and thus do not present any concerns.
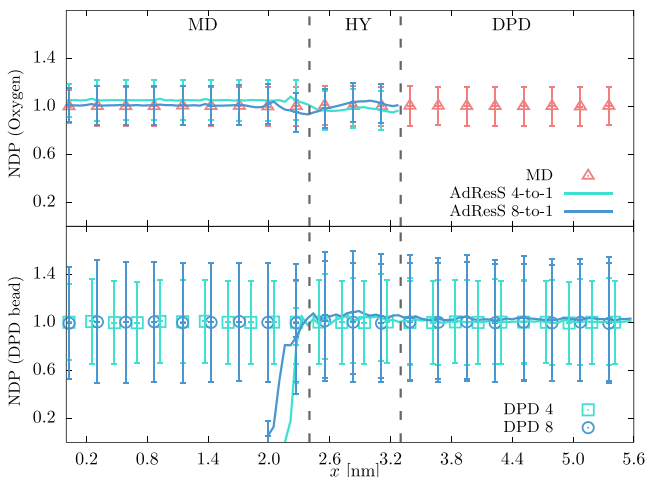

FIG. 4. Normalized density profiles (NDPs) with standard deviations for water oxygen atoms (top) and DPD beads (bottom). The multiscale AdResS simulations results match well the conventional MD and DPD simulations. Vertical lines mark the domains of MD and DPD methods.
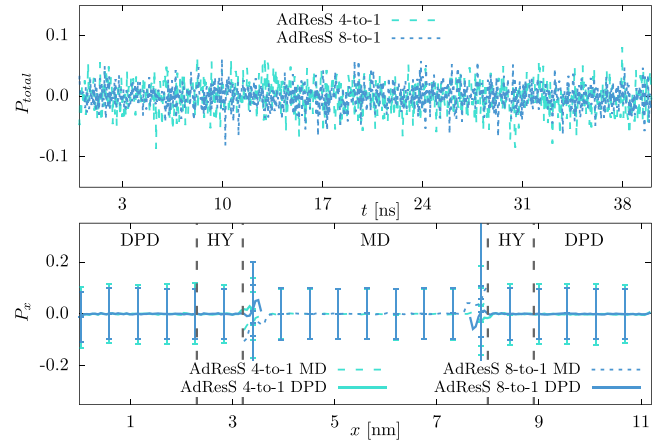

FIG. 5. Top: Total linear momentum P_{total} as a function of time. For comparison, the results are also shown for the case when the TD force is applied to pure DPD simulations. Bottom: Local total linear momentum P_x with standard deviations as a function of position in the simulation box computed for atoms (MD) and DPD particles in the relevant domains. Both linear momentums are in units of nm/ps and scaled with the system's total mass.

One of the advantages of coupling to DPD method is the conservation of the linear momentum, that is in general not conserved using global (such as Nosé-Hoover[58]) or local, e.g., Langevin,[59] thermostats. The magnitude of the total momentum, computed as a center-of-mass velocity $\boldsymbol{P}_{total} = \left(\sum_{i \in MD} m_i \boldsymbol{v}_i + \sum_{\alpha \in DPD,HY} M_\alpha \boldsymbol{V}_\alpha\right) \big/ \left(\sum_{i \in MD} m_i + \sum_{\alpha \in DPD,HY} M_\alpha\right)$, is shown in Fig. 5. Note that the system is symmetric over the center of simulation box, i.e., we have two HY regions and thus the applied TD force is symmetric over the center of simulation box center, too. Hence, the total momentum is preserved owing to the translational invariance achieved by periodic boundary conditions. To further demonstrate this point, we also show the results where the TD force is applied to the pure DPD simulations. As already mentioned above, the AdResS force coupling scheme strictly conserves the local linear momentum [Eq. (3)]. However, the extended coupling scheme with the TD force [Eq. (5)] conserves the linear momentum locally only on the fluctuating hydrodynamics level. To validate this statement, we show, in Fig. 5, the x component of the local linear momentum P_x after binning the particles (either atoms or DPD particles) according to their position along the x-axis, where $P_x(x) = \sum_i m_i v_{x,i} \delta(x_i - x) / \sum_i m_i \delta(x_i - x)$ in the MD domain and $P_x(x) = \sum_\alpha M_\alpha V_{x,\alpha} \delta(X_\alpha - x) / \sum_\alpha M_\alpha \delta(X_\alpha - x)$ in the DPD domain. The local linear momentum is zero (corresponding to no momentum flux) with some deviations in the cluster formation region due to external TD force that violates Newton's third law. However, these deviations are smaller than the error bars. This result demonstrates that our multiscale approach conserves also the local linear momentum.

Information about the equilibrium structural and dynamical organization of water can be extracted from the Van Hove function $G(\boldsymbol{r}, t)$, which is a correlation function of position and time defined for homogeneous medium as

$$G(\boldsymbol{r}, t) = N^{-1} \sum_{i,j} \langle \delta(\boldsymbol{r} + \boldsymbol{r}_j(0) - \boldsymbol{r}_i(t)) \rangle. \qquad (8)$$

The double sum is performed over all pairs of N particles in the system, $\boldsymbol{r}_{i,j}(t)$ is the position vector of the i, j-th particle
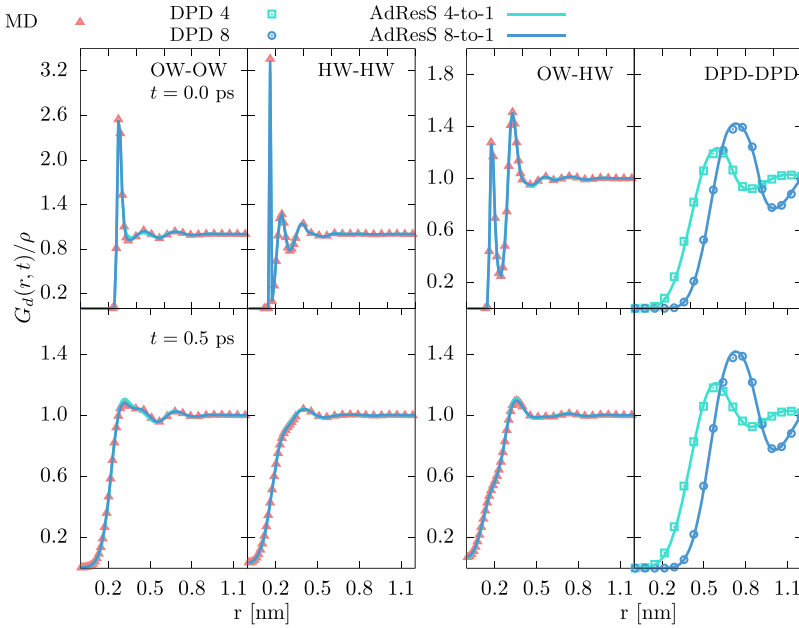
FIG. 6. Distinct part of the Van Hove function $G_d(r,t)/\rho$ at times 0.0 (top) and 0.5 ps (bottom) for the oxygen-oxygen (OW-OW), oxygen-hydrogen (OW-HW), hydrogen-hydrogen (HW-HW), and DPD-DPD case.

at time t, and the brackets $\langle \ldots \rangle$ denote an average over time origins. By differentiating between the cases $i = j$ and $i \neq j$, the $G(r,t)$ can be separated into two terms, usually referred to as the self and distinct parts, respectively. In Fig. 6, we first examine the distinct part G_d, which gives the probability to find a different particle at position $\boldsymbol{r}$ at time t, given that there was a particle at the origin at time $t = 0$. For isotropic fluids, the G_d depends only on the scalar quantity r and can thus be computed as

$$G_d(r,t) = (4\pi r^2 N)^{-1} \sum_{i \neq j} \langle \delta(r - |\boldsymbol{r}_i(t) - \boldsymbol{r}_j(0)|)\rangle. \quad (9)$$

At $t = 0$ the G_d relates to the well-known radial distribution function $G_d(r,0) = \rho g(r)$. We calculated the distinct part of Van Hove function for water oxygen-oxygen, oxygen-hydrogen, hydrogen-hydrogen, and DPD-DPD at two different

times: 0 and 0.5 ps (Fig. 6 top and bottom plots, respectively). To make a relevant comparison with the reference simulations, the Gds are computed locally for the multiscale simulations, i.e., we only consider the molecules either in the MD or DPD domain. We then compare the Gds from the MD domain of the AdResS setup with the corresponding Gds from fully MD simulations, whereas the Gds from the DPD domain of the AdResS setup are compared with the corresponding ones from fully DPD simulations. For both AdResS simulations, all G_d match the reference results within the line thickness thus demonstrating that, in equilibrium, not only the structural part but also the dynamical part of the water organization is fully preserved in both domains.

The self part of the Van Hove function $G_s(r,t)$ for water oxygen atoms and DPD particles is shown in Fig. 7 from 0.5 to 5 ps. The $G_s(r,t)$, given by
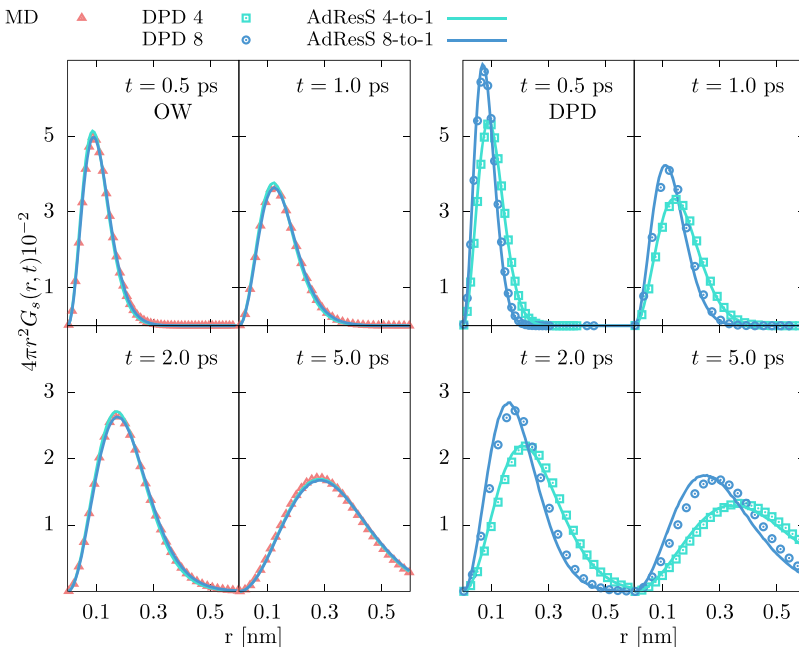

FIG. 7. Self part of the Van Hove function $4\pi r^2 G_s(r,t)$ for water oxygen (OW) atoms and DPD particles at times 0.5, 1.0, 2.0, and 5.0 ps.

$$G_s(r,t) = (4\pi r^2 N)^{-1} \sum_i \langle \delta(r - |\mathbf{r}_i(t) - \mathbf{r}_i(0)|) \rangle, \qquad (10)$$

probes the equilibrium dynamics of a single particle in terms of its displacement from an initial position. AdResS simulations again give very comparable results to the reference simulations.

Next, we analyze the behavior of four different order parameters. We report, in Fig. 8, the first two $\eta^{1,2}$ that probe the orientational distribution of water molecules. We define them as $\eta^l(x) = \langle P_l(\hat{\boldsymbol{\mu}}\hat{\boldsymbol{n}}) \rangle$, where P_l is the Legendre polynomial of the order l, $\hat{\boldsymbol{\mu}}$ is the unit vector along the water's dipole moment, and $\hat{\boldsymbol{n}}$ is the unit vector pointing in the x direction. The brackets $\langle \ldots \rangle$ denote averaging over the trajectory and water molecules that are located in a bin centered around x. A random orientation of water molecules, corresponding to $\eta^{1,2} = 0$, is observed in the MD region, whereas some preferential orientation is observed in the HY region. With the third order parameter η^3, we explore the water quadrupolar moment in the x direction defined by $\eta^3(x) = \langle \sum_i q_i r_i r_i \rangle$, where the index i runs over the water hydrogens with charge q_i and at distance r_i in the x direction with respect to the position of the oxygen atom of the considered water molecule.

The profile of the fourth order parameter $Q_4(x) = \langle 1 - 3/8 \sum_{i=1}^3 \sum_{j=i+1}^4 (\cos\theta_{ijk} + 1/3)^2 \rangle$, water's tetrahedrality, is shown Fig. 9. The sum runs over distinct pairs of the four closest neighbors of the reference water molecule i and θ_{ijk} is the angle between vectors $\mathbf{r}_{ij}$ and $\mathbf{r}_{ik}$ with j and k being the nearest neighbor molecules. This parameter measures the degree of tetrahedral order, with $Q_4 = 1$ corresponding to the perfect tetrahedral arrangement and $Q_4 = 0$ to an ideal gas. In the MD region, the bulk value $Q_4^{\text{bulk}} = 0.6$ is well reproduced. In the HY region, the presence of half-harmonic bonds between oxygen atoms, as expected, distorts the local structure of water. In addition, the MD interactions are gradually switched off, which affects the hydrogen bonding. Thus, we observe a continuous decrease of the Q_4 parameter as we move away from the MD

FIG. 9. Local tetrahedral order parameter Q_4 (top) and dielectric permittivity (bottom) as a function of x coordinate of the simulation box.

region. Due to the same reasons, deviations from the bulk are also observed in the water's dielectric permittivity, which we calculate within the Kirkwood theory where it is related to the average vector sum of the dipole moments of a water molecule centered in a spherical region embedded into a solvent continuum.[30]

We analyze the reorientation dynamics of water by means of autocorrelation functions of the single water molecule dipole moment defined by $C_\mu^l(t) = \langle P_l[\hat{\boldsymbol{\mu}}(0)\hat{\boldsymbol{\mu}}(t)] \rangle$, where $\hat{\boldsymbol{\mu}}(t)$ is the unit dipole vector at time t, P_l are the Legendre polynomials, while the brackets $\langle \ldots \rangle$ indicate average over time origins and water molecules. The obtained autocorrelation functions for the first Legendre polynomial are reported in Fig. 10. Additionally, we report the velocity autocorrelation functions for oxygen atoms and DPD particles. The AdResS simulations agree very well with the reference fully MD simulation, whereas some deviations are observed in the agreement with the DPD simulations for the
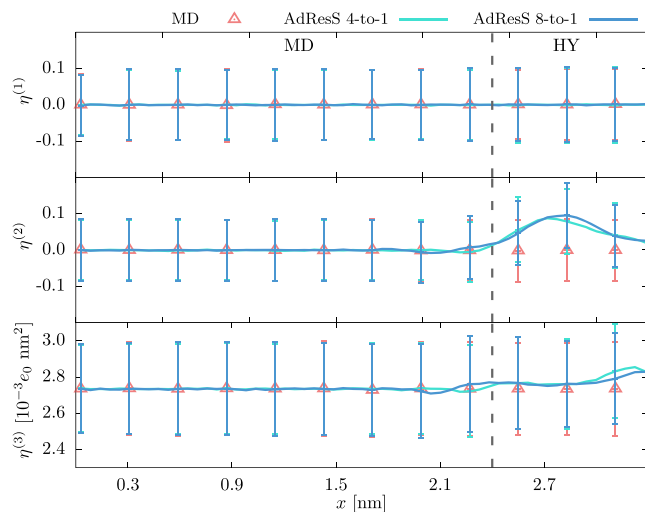

FIG. 8. Order parameters $\eta^{1,2,3}$ of water molecules as a function of position in the simulation box. The error bars represent the standard deviation of the measurements. The results are shown for the AdResS and MD simulations. Vertical lines mark the boundary between the MD and HY domains.
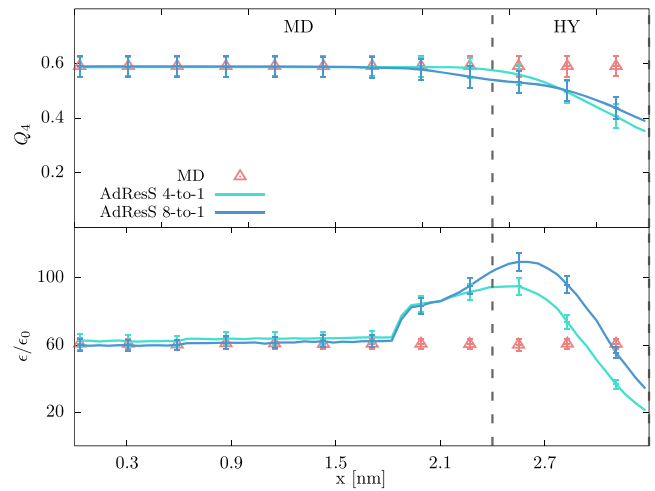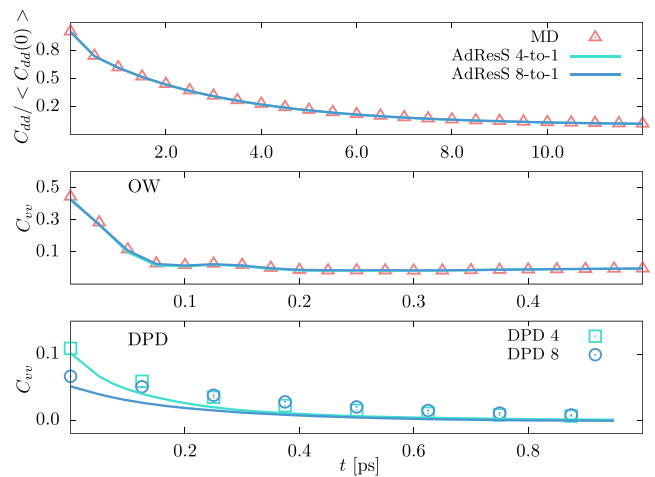

FIG. 10. Top: Single water molecule reorientation measured by the normalized dipole autocorrelation function. Middle and bottom: Velocity autocorrelation function for oxygen atoms and DPD particles, respectively. For the AdResS simulations, we average over molecules that are at time $t = 0$ located within the relevant region.[60]

DPD velocity autocorrelation functions as further discussed below.

Finally, we compute the diffusion via mean square displacements (MSD). Figure 11 shows MSDs for MD and DPD monoscale simulations computed for oxygen atoms and DPD beads, respectively. The diffusion constants D of the DPD models are higher than the MD counterparts due to softer interaction potentials. The value of D is ≈ 1.7 times higher for the DPD simulations with 4-to-1 mapping compared with the 8-to-1 mapping. This result is in accordance with Ref. 33, where D was systematically investigated for a number of mappings N_m. There, D was found to gradually decrease with N_m with a scaling factor of ≈ 1.8 between $N_m = 4$ and 8. For comparison, the value of D for the MARTINI water model, which is using a 4-to-1 mapping, is 1.92×10^{-9} m^2 s^{-1},[61] while for the DPD at the same mapping we obtain $(7.7 \pm 0.2) \times 10^{-9}$ m^2 s^{-1}. This difference by a factor of 4 is due to stiffer interactions used in the MARTINI model, i.e., the Lennard-Jones interaction.[17] If we wanted to match the DPD diffusion constants to MD ones we would have to resort to the transverse DPD thermostat strategy.[13] In AdResS simulations, the water atoms and DPD beads are only defined in a certain region. Thus, special consideration is needed to compute the MSDs in our case.[60] In particular, to compute the MSD of oxygen atoms we average only over oxygen that were within a given time scale (50 ps) always located within the MD region. Similarly, the MSDs for DPD particles are averaged only over DPD particles continuously residing in the DPD region. For oxygen, the diffusion coefficient of AdResS simulations agrees well with monoscale MD result and with the one reported in the literature.[62] For DPD particles, we observe somewhat lower diffusion in the AdResS simulations compared with monoscale DPD simulation due to the coupling to the MD region and consequent additional friction felt by DPD particles at the HY/DPD boundary. Note, that the same effect can be seen from velocity autocorrelation functions in Fig. 10. The diffusion coefficient for the oxygen obtained from the velocity autocorrelation functions are (4.5 ± 0.2) (4.1 ± 0.2), and

$(4.4 \pm 1.4) \times 10^{-9}$ m^2 s^{-1} for the MD, AdResS 4-to-1, and AdResS 8-to-1 simulations, respectively. For the DPD diffusion, we obtain (8.5 ± 0.3) (8.4 ± 0.5), (5.2 ± 0.2), and (3.2 ± 1) $\times 10^{-9}$ m^2 s^{-1} for the DPD 4, DPD 8, AdResS 4-to-1, and AdResS 8-to-1 simulations, respectively. The values of D from MSDs and velocity autocorrelation functions approximately match.

IV. CONCLUSIONS AND OUTLOOK

We have presented the coupling of MD and DPD simulation techniques and validated our approach by demonstrating that the multiscale systems can in respective domains fully reproduce the statistical properties of the conventional monoscale simulations. Both coupled methods, i.e., the MD with the DPD thermostat and the DPD, and the coupling algorithm AdResS guarantee by construction the local linear momentum conservation. In the extended version of AdResS with the TD force, which is needed to compensate the chemical potential differences of the coupled models, the local linear momentum is no longer conserved on the microscopic level. However, it is locally conserved on the fluctuating hydrodynamics level and, therefore, our approach nevertheless properly reproduces momentum propagation, which is necessary for correct reproduction of hydrodynamic behavior.[12] As a benchmark system, we used bulk water employing a supramolecular coupling, where either 4 or 8 water molecules are represented as soft blobs in the DPD domain. For the 8-to-1 mapping, we extended our previous methodology to the supramolecular coupling of beyond nearest neighbor molecules. The employed methodology is general and can be applied to any N-to-1 mapping, with N going up to 20 (the upper limit is imposed by the DPD model). Furthermore, we considered the reversed definition of the weighting function, which enabled the elimination of the additional atomistic region of bundled water. To facilitate future applications, we used DPD water models that had been previously employed in simulations of phospholipid membranes[41] and polymer melts,[42] thus making the multiscale models applicable to biophysical as well as technological applications. The framework could also be used in the important studies of abnormal rheological and biomechanical properties of red blood cells encountered in disease states.[63–67] In our future work, we will apply the presented multiscale methodology to fluid flow simulations (see for example Refs. 68–70) to explore its advantages and limitations to properly capture hydrodynamics. Furthermore, we will open up the boundaries of a molecular system and allow for the exchange of matter with its surrounding using Open Boundary Molecular Dynamics (OBMD).[48–50] In doing so, we will be able to validate whether the fluctuating details, e.g., relative mass fluctuations, are preserved across the MD-DPD interface.
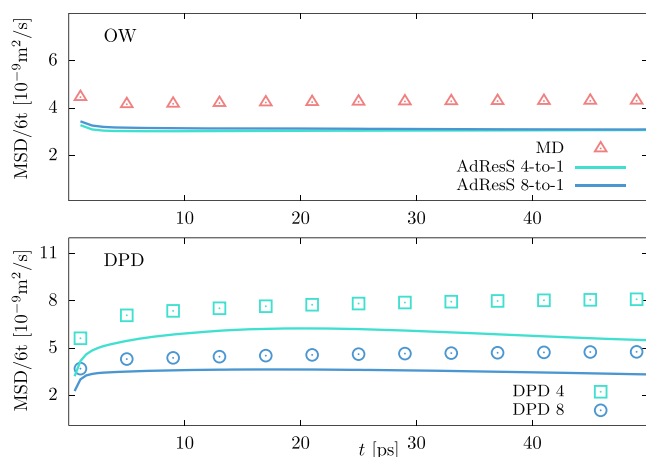

FIG. 11. Diffusion coefficients, i.e., mean square displacements (MSD) divided by $6t$, computed for oxygen atoms (top) and DPD beads (bottom). For the AdResS simulations, we average only over particles that are located within the specific region (MD for oxygen atoms and DPD for DPD particles) continuously within 50 ps.

ACKNOWLEDGMENTS

[1]R. D. Groot and P. B. Warren, J. Chem. Phys. **107**, 4423 (1997).
[2]P. Español, Phys. Rev. E **52**, 1734 (1995).
[3]P. Español and P. B. Warren, J. Chem. Phys. **146**, 150901 (2017).
[4]P. J. Hoogerbrugge and J. M. V. A. Koelman, Europhys. Lett. **19**, 155 (1992).
[5]P. Español and P. B. Warren, Europhys. Lett. **30**, 191 (1995).
[6]E. K. Peter and I. V. Pivkin, J. Chem. Phys. **141**, 164506 (2014).
[7]P. B. Warren and A. Vlasov, J. Chem. Phys. **140**, 084904 (2014).
[8]R. D. Groot, J. Chem. Phys. **118**, 11265 (2003).
[9]A. Malevanets and R. Kapral, J. Chem. Phys. **110**, 8605 (1999).
[10]P. Espanol and M. Revenga, Phys. Rev. E **67**, 026705 (2003).
[11]A. Vázquez-Quesada, M. Ellero, and P. Espanol, J. Chem. Phys. **130**, 034901 (2009).
[12]T. Soddemann, B. Dunweg, and K. Kremer, Phys. Rev. E **68**, 046702 (2003).
[13]C. Junghans, M. Praprotnik, and K. Kremer, Soft Matter **4**, 156 (2008).
[14]C. Hijón, P. Español, E. Vanden-Eijnden, and R. Delgado-Buscalioni, Faraday Discuss. **144**, 301 (2010).
[15]S. Izvekov, J. Chem. Phys. **146**, 124109 (2017).
[16]Z. Li, X. Bian, B. Caswell, and G. E. Karniadakis, Soft Matter **10**, 8659 (2014).
[17]Z. Li, X. Bian, X. Li, and G. E. Karniadakis, J. Chem. Phys. **143**, 243128 (2015).
[18]L. Gao and W. Fang, J. Chem. Phys. **135**, 184101 (2011).
[19]G. Jung, M. Hanke, and F. Schmid, J. Chem. Theory Comput. **13**, 2481 (2017).
[20]S. Matysiak, C. Clementi, M. Praprotnik, K. Kremer, and L. Delle Site, J. Chem. Phys. **128**, 024503 (2008).
[21]J. W. Wagner, J. F. Dama, A. E. P. Durumeric, and G. A. Voth, J. Chem. Phys. **145**, 044108 (2016).
[22]J. F. Dama, J. Jin, and G. A. Voth, J. Chem. Theory Comput. **13**, 1010 (2017).
[23]M. Praprotnik, L. Delle Site, and K. Kremer, J. Chem. Phys. **123**, 224106 (2005).
[24]M. Praprotnik, L. Delle Site, and K. Kremer, Annu. Rev. Phys. Chem. **59**, 545 (2008).
[25]M. Praprotnik, S. Poblete, and K. Kremer, J. Stat. Phys. **145**, 946 (2011).
[26]R. Potestio, S. Fritsch, P. Español, R. Delgado-Buscalioni, K. Kremer, R. Everaers, and D. Donadio, Phys. Rev. Lett. **110**, 108301 (2013).
[27]R. Potestio, P. Español, R. Delgado-Buscalioni, R. Everaers, K. Kremer, and D. Donadio, Phys. Rev. Lett. **111**, 060601 (2013).
[28]H. Wang, C. Hartmann, C. Schütte, and L. Delle Site, Phys. Rev. X **3**, 011018 (2013).
[29]A. Cameron, J. Chem. Phys. **123**, 234101 (2005).
[30]J. Zavadlav, R. Podgornik, and M. Praprotnik, J. Chem. Theory Comput. **11**, 5035 (2015).
[31]N. D. Petsev, L. G. Leal, and M. S. Shell, J. Chem. Phys. **142**, 044101 (2015).
[32]U. Alekseeva, R. G. Winkler, and G. Sutmann, J. Comput. Phys. **314**, 14–34 (2016).
[33]I. V. Pivkin and G. E. Karniadakis, J. Chem. Phys. **124**, 184101 (2006).
[34]J. Zavadlav, M. N. Melo, A. V. Cunha, A. H. de Vries, S. J. Marrink, and M. Praprotnik, J. Chem. Theory Comput. **10**, 2591 (2014).
[35]J. Zavadlav, M. N. Melo, S. J. Marrink, and M. Praprotnik, J. Chem. Phys. **142**, 244118 (2015).
[36]S. M. Gopal, A. B. Kuhn, and L. V. Schäfer, Phys. Chem. Chem. Phys. **17**, 8393 (2015).
[37]J. Zavadlav, S. J. Marrink, and M. Praprotnik, J. Chem. Theory Comput. **12**, 4138 (2016).

[38]J. Zavadlav, M. N. Melo, S. J. Marrink, and M. Praprotnik, J. Chem. Phys. **140**, 054114 (2014).
[39]J. Zavadlav, R. Podgornik, M. N. Melo, S. J. Marrink, and M. Praprotnik, Eur. Phys. J.: Spec. Top. **225**, 1595 (2016).
[40]S. J. Marrink and D. P. Tieleman, Chem. Soc. Rev. **42**, 6801 (2013).
[41]X. Li, L. Gao, and W. Fang, PLoS One **11**, e0154568 (2016).
[42]D. Nikolić, K. A. Moffat, V. M. Farrugia, A. E. Kobryn, S. Gusarov, J. H. Wosnick, and A. Kovalenko, Phys. Chem. Chem. Phys. **15**, 6128 (2013).
[43]H. J. C. Berendsen, J. P. M. Postma, W. F. van Gunsteren, and J. Hermans, Intermol. Forces **14**, 331 (1981).
[44]S. Miyamoto and P. A. Kollman, J. Comput. Chem. **13**, 952 (1992).
[45]M. Neumann, J. Chem. Phys. **82**, 5663 (1985).
[46]D. Reith, M. Pütz, and F. Müller-Plathe, J. Comput. Chem. **24**, 1624 (2003).
[47]S. Bevc, C. Junghans, and M. Praprotnik, J. Comput. Chem. **36**, 467 (2015).
[48]R. Delgado-Buscalioni, J. Sablić, and M. Praprotnik, Eur. Phys. J.: Spec. Top. **224**, 2331 (2015).
[49]J. Sablić, M. Praprotnik, and R. Delgado-Buscalioni, Soft Matter **12**, 2416 (2016).
[50]J. Sablić, M. Praprotnik, and R. Delgado-Buscalioni, Soft Matter **13**, 4971 (2017).
[51]S. Poblete, M. Praprotnik, K. Kremer, and L. Delle Site, J. Chem. Phys. **132**, 114101 (2010).
[52]S. Fritsch, S. Poblete, C. Junghans, G. Ciccotti, L. Delle Site, and K. Kremer, Phys. Rev. Lett. **108**, 170602 (2012).
[53]L. Delle Site and M. Praprotnik, Phys. Rep. **693**, 1 (2017).
[54]P. Español, R. Delgado-Buscalioni, R. Everaers, R. Potestio, D. Donadio, and K. Kremer, J. Chem. Phys. **142**, 064115 (2015).
[55]R. Delgado-Buscalioni, Philos. Trans. R. Soc., A **374**, 20160152 (2016).
[56]R. Everaers, Eur. Phys. J.: Spec. Top. **225**, 1483–1503 (2016).
[57]J. D. Halverson, T. Brandes, O. Lenz, A. Arnold, S. Bevc, V. Starchenko, K. Kremer, T. Stuehn, and D. Reith, Comput. Phys. Commun. **184**, 1129 (2013).
[58]W. G. Hoover, Phys. Rev. A **31**, 1695 (1985).
[59]G. S. Grest and K. Kremer, Phys. Rev. A **33**, 3628 (1986).
[60]L. Delle Site, Phys. Rev. E **93**, 022130 (2016).
[61]M. Fuhrmans, B. P. Sanders, S. J. Marrink, and A. H. de Vries, Theor. Chem. Acc. **125**, 335 (2010).
[62]D. van der Spoel, P. J. van Maaren, and H. J. C. Berendsen, J. Chem. Phys. **108**, 10220 (1998).
[63]H. Chang, X. Li, H. Li, and G. E. Karniadakis, PLoS Comput. Biol. **12**, e1005173 (2016).
[64]A. M. Altenhoff, J. H. Walther, and P. Koumoutsakos, J. Comput. Phys. **225**, 1125 (2007).
[65]D. Rossinelli, Y.-H. Tang, K. Lykov, D. Alexeev, M. Bernaschi, P. Hadjidoukas, M. Bisson, W. Joubert, C. Conti, G. Karniadakis *et al.*, in *Proceedings of the International Conference for High Performance Computing, Networking, Storage and Analysis* (ACM, New York, 2015), p. 2.
[66]D. A. Fedosov, B. Caswell, and G. E. Karniadakis, Biophys. J. **98**, 2215 (2010).
[67]D. A. Fedosov, W. Pan, B. Caswell, G. Gompper, and G. E. Karniadakis, Proc. Natl. Acad. Sci. U. S. A. **108**, 11772 (2011).
[68]R. Delgado-Buscalioni, K. Kremer, and M. Praprotnik, J. Chem. Phys. **128**, 114110 (2008).
[69]R. Delgado-Buscalioni, K. Kremer, and M. Praprotnik, J. Chem. Phys. **131**, 244107 (2009).
[70]J. H. Walther, M. Praprotnik, E. M. Kotsalis, and P. Koumoutsakos, J. Comput. Phys. **231**, 2677 (2012).